

Electrodeposition of Fe–W Alloys from Citrate Bath: Impact of Anode Material

S. S. Belevskii^a, V. V. Danilchuk^b, A. V. Gotelyak^b, M. Lelis^c, S. P. Yushchenko^a, and A. I. Dikusar^{a, b, *}

^a*Institute of Applied Physics, Chisinau, MD-2028 Moldova*

^b*Shevchenko Pridnestrovie State University, Tiraspol, MD-3300 Moldova*

^c*Lithuanian Energy Institute, Kaunas, LT-44403 Lithuania*

**e-mail: aidikusar@gmail.com*

Received August 18, 2018; revised August 19, 2019; accepted August 19, 2019

Abstract—The effect of the anode material on the rate of electrodeposition of Fe–W alloy coatings from a citrate bath is studied. Both Fe and Ni soluble anodes and Pt and graphite insoluble anodes are addressed. The effects associated with the anode material are attributed to anodic oxidation of an Fe(II)–citrate complex involved in electrodeposition. In addition to its likely oxidation at the anode, this complex catalyzes reduction of W-containing species and acts as precursor to Fe deposition; these processes unfold via the formation of corresponding intermediates, their surface coverage determining the alloy composition. X-ray photoelectron spectroscopy characterization of deposited alloys indicates that the intermediate FeOH_{ads} is oxidized by water to form surface oxides. This process can explain the previously reported macroscopic size effect, i.e., the effect of the volume current density on the microhardness of deposited alloys. By using a soluble iron anode, we achieve an unprecedentedly high rate of alloy deposition (25 $\mu\text{m}/\text{h}$ at a current density of 20 mA/cm^2).

Keywords: electrodeposition, Fe–W alloys, anode, volume current density, macroscopic size effect, x-ray photoelectron spectroscopy, iron–citrate complexes, microhardness

DOI: 10.3103/S1068375520010020

INTRODUCTION

Electrodeposition of alloys between the iron group metals and refractory metals (W, Mo, and Re) in the bulk form or thin films, or quasi-one-dimensional structures (e.g., nanowires, nanotubes, and nanoribbons) is a growing area of research. Such materials and structures show a great promise due to their unique anticorrosive, strengthening, catalytic, and magnetic properties [1–3]. Interest to such materials, which are obtained by electrochemical deposition, is not limited to their use in real-life applications. It has been repeatedly remarked that electrodeposition of such alloys has a number of important features [1]. For instance, tungsten cannot be deposited from aqueous baths while, with a salt of an iron group metal added to an electrodeposition bath, an alloy with a tungsten content of as high as 50 wt % can be obtained. Electrodeposition of this type is known as induced codeposition [1, 2, 4–6].

The properties of materials under discussion (e.g., microhardness) are subject to so-called macroscopic size effect, and this can be considered as a specific feature of electrodeposition of such alloys [7–12]. In particular, this effect consists in the following: the microhardness of a deposited coating depends not only on the bath composition, temperature, pH, and applied

current density (or potential), but also on the deposition surface area. This actually means that, in addition to well-known parameters used in electrochemistry, the volume current density (VCD) can be used to control the properties of deposited materials (in the case investigated here—microhardness) since the VCD grows with enlarging the deposition surface area, if the applied deposition current density and the electrolyte volume are kept constant. It seems obvious that anomalies of this kind will remain puzzling until the mechanism underlying this type of electrodeposition is fully understood. Unfortunately, so far the mechanism of induced codeposition has remained a matter for debate [1, 2, 5, 6, 13–15].

Fe–W alloy coatings obtained by electrodeposition are important representatives of the considered types of alloys [16–25]. New prospects for using these materials in their bulk form [1, 2, 4, 16, 17, 23–25] or in the form of quasi-one-dimensional structures [3] have been investigated elsewhere. It is necessary to highlight that baths typically used for electrodeposition of alloys between the iron group metals and refractory metals are ecologically benign (mainly, these are citrate or gluconate baths with a neutral pH). However, there is a problem with electrodeposition of Fe–W coatings: because the added bivalent iron spe-

cies undergo oxidation, the bath exhibits loss of stability and loss of performance. Iron was believed to be oxidized by dissolved oxygen [25, 26]. However, another study found that the oxidation occurred even under an inert gas atmosphere [27]. This difficulty can be overcome by using citrate–ammonia baths [20, 21, 28, 29], but this has a negative impact on the ecological aspect of technology. Attempts to avoid the use of ammonia in plating baths, or, at least, considerably reduce its content, were reported [24, 25, 30–32]. To improve the performance of electroplating baths under discussion, an ecologically friendly citrate–glycolate bath (i.e., a bath containing glycolic acid) based on trivalent iron was developed in [25, 32]. That plating bath made it possible to control the composition of deposited coatings and their mechanical and magnetic properties, as well as to achieve rather high deposition rates (17 $\mu\text{m/h}$ at a current density of 20 mA/cm^2).

Unfortunately, the use of glycolic acid raises the costs of the coating fabrication technology considerably. It is therefore reasonable to develop technologies for fabrication of Fe–W coatings and structures using ecologically benign glycolate-free citrate baths. This problem, in particular, was addressed in studies [26, 27, 33]. Crucially, a bath used in the cited works for electrodeposition of such coatings was a mixture of citrate complexes of bi- and trivalent iron, apart from tungsten complexes, while initially only a salt of bivalent iron was used as iron-containing bath component. This bath enabled electrodeposition of quality coatings with high hardness at a current efficiency of 32–37% (assuming alloy formation from Fe(II) species) using insoluble anodes (graphite and stainless steel) [26, 27].

We note that the electrodeposition techniques under discussion typically produce nanocrystalline coatings. In contrast to electroplated iron, incorporation of W, even in small amounts, was found to lead to the formation of nanocrystalline coatings [25]. The microhardness of those coatings, which is determined by the sizes of nanocrystallites, depends on the W content in the coatings [32]. The electrodeposition technology, however, requires further development, since currently attainable deposition rates are relatively low. Electrodeposition rates in, and performance of, baths for plating alloys between the iron group metals and tungsten can potentially be improved by using soluble anodes [8, 9, 11, 33]. The current efficiency of anodic dissolution of iron in citrate baths for electroplating of Fe–W alloys was shown to be close to 100% in a broad range of current densities [27, 33], suggesting that iron can be a proper material for soluble anodes in these processes. A study [33] addressing electrodeposition of Fe–W coatings from a citrate bath using a soluble iron anode identified that the use of this anode ensured higher current efficiencies and electrodeposition rates, and, under particular conditions, longer usage time of the bath and stability of its operational parameters during extended electrolysis.

This work aims at identifying: (i) the effects that anodic process have on the rate of electrodeposition and properties of Fe–W coatings deposited from a citrate bath, (ii) the nature of these effects, and (iii) the conditions favoring efficient use of soluble anodes. The inquiry along these lines should provide a control over the deposition rate and properties of electrodeposited Fe–W alloys.

EXPERIMENTAL

A citrate bath used in this study contained FeSO_4 (0.2 M), Na_2WO_4 (0.4 M), citric acid (0.17 M), and trisodiumcitrate (0.33 M). The bath pH was 6.9 and depositions were carried out at 80°C. The bath was prepared by, first, dissolving iron(II) sulfate (heptahydrate) in the citrate buffer prepared beforehand, followed by dissolving sodium tungstate (dihydrate) in the resulting solution. This electrolyte was used as plating bath in our studies concerning electrodepositions onto copper and steel substrates using a galvanostatic control and onto a platinum wire electrode using potentiostatic control, as well as for studying electrode processes by cyclic voltammetry (CV).

Electrodepositions were carried out in the galvanostatic mode from quiescent solutions at applied current densities in the range of 5 to 100 mA/cm^2 using a 0.5 L cell and different anodes: an insoluble graphite (Type TM-3) anode as well as soluble iron (St3 steel) and nickel (Type N1) ones. For each deposition, substrates were plated with a nickel sublayer, $\sim 0.5 \mu\text{m}$ thick, from a bath containing $\text{NiCl}_2 \cdot 6\text{H}_2\text{O}$ (240 g/L) at pH 2 and current density of 30 mA/cm^2 ; electrolysis duration was 60 s. A series of experiments in which the graphite anode was used were carried out in a cell with separate cathode and anode compartments. A MF microfiltration membrane with an average pore diameter of 0.74 μm (produced in Dubna, Russia) was used as separating membrane in this cell.

To investigate redox processes involved in electrodepositions with different anodes, CV and potentiostatic electrodeposition (i.e., the electrode potential was fixed during these experiments) were used. CV was performed in a three-electrode cell using a Pt wire electrode (area, 0.159 cm^2) as the working electrode, an Ag/AgCl (sat.) reference electrode, while the counter electrode was made of different materials (Pt, graphite, and Fe). Henceforth, all of the potentials are cited relative to the Ag/AgCl (sat.) electrode. A soluble iron anode was made of soft steel, Type St3. For CV measurements and potentiostatic depositions, the area of the counter electrode was considerably larger than that of the working electrode (i.e., platinum wire); the scan rate was 10 mV/s. Potential scans were started in the cathodic direction from the open circuit potential to a potential of -1.3 V and then in the anodic direction to $+0.7 \text{ V}$. As a side note, the potential sweep directions are indicated on CVs. All CV measurements

were conducted at a temperature of 80°C in the citrate bath described above. Prior to measurements, the Pt electrode was subjected to an anode–cathode pre-treatment: in a two-electrode cell, the electrode was poised at a potential of +1 V in ~ 30% nitric acid for a time (the other electrode was a large-area platinum electrode), and then the potential was set to –0.2 V until the first cathodic current peak was passed.

To investigate the effects of anodic processes on the electrodeposition rate and the current efficiency of the cathodic process, we carried out a long (2 h) potentiostatic deposition of a Fe–W alloy onto the Pt wire electrode at an applied potential of –1.05 V using the anodes made of different materials (Pt, St3, and graphite), followed by a potentiostatic control of the diffusion-limited current density of the reduction of an Fe(III)–citrate complex. This current density was shown to control the rate of a side reduction process that runs in parallel to the main process, i.e. the reduction leading to alloy deposition, and has a considerable impact on the current efficiency of the alloy deposition process. The reduction current density was determined at a potential of –0.5 V. In doing so, a Pt electrode with a larger area was used.

The rates of the electrochemical process, i.e., current densities, were calculated with respect to the geometric surface area of the Pt wire electrode. The measurements were conducted using a PARSTAT 2273 potentiostat controlled by the Power Suite V 2.58 software.

To establish the distribution of deposition rates and the surface properties for depositions with different anodes (iron or graphite), we used a Hull cell with a rotating cylinder electrode (RCE) in a described previously configuration [7, 34, 35]. A cylinder electrode with a diameter of 30 mm and a height of the working part $H = 30$ mm was used for experiments in quiescent solutions or was rotated at a rate in the range of 270–570 rpm; in the latter case the Reynolds numbers (Re) were in the range of $\sim(1-2) \times 10^3$, which corresponded to a turbulent flow regime. Under these flow conditions, the width of the concentration gradient layer was uniform across the entire length of the cylinder electrode. Electrodeposition was performed at two average current densities of 20 and 40 mA/cm². The primary current distribution for our RCE/cell geometry is given in Table 1. Clearly, the maximal primary current density is at a point close to the anode ($x/H = 0.1$) while the minimal current density is at a point most remote from the anode ($x/H = 0.91$; Table 1). We can see that the current density changes by a factor of 12. An actual current distribution is not so extreme due to the effects associated with the secondary current distribution (overvoltage and surface processes). We can also see that the mean current density (i.e., 20 or 40 mA/cm²) is reached at $x/H = 0.37$ (Table 1). Despite that an actual current distribution differs from the data in Table, we anticipate that the effect of a (local) current density on the electrodeposition rate

Table 1. Distribution of primary current density along a rotating cylinder electrode placed in a Hull cell

Point no.	x/h	Average current density, mA/cm ²	
		20	40
1	0.10	60	120
2	0.24	40	80
3	0.37	20	40
4	0.51	15	30
5	0.64	10	20
6	0.77	6.6	13
7	0.91	5	10

and the composition and microhardness of deposited coatings can be evaluated by determining the thickness, composition, and properties (microhardness) of these coatings in relation to the type of the anode (graphite or iron) and the hydrodynamic conditions used.

The chemical composition of the fabricated coatings was determined on a Hitachi TM360 scanning electron microscope (SEM) equipped with an attachment for energy-dispersive X-ray spectroscopy (EDS). X-ray photoelectron spectroscopy (XPS) characterizations of our Fe–W coatings were performed using a ULVAC-PHI Versaprobe instrument. The coating microhardness was measured on a PMT-3 microhardness tester using a Vickers indenter and a load of 100 g. At least three measurements were carried out for each sample, and the values provided here are the mean values with standard deviations.

RESULTS AND DISCUSSION

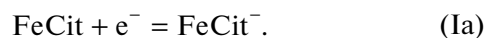
Key Potentials Characterizing Electrodeposition of Fe–W Alloys: Elucidating Roles of Redox Processes and Anode

A CV profile characteristic of the considered electrochemical system (Fig. 1) can be used to identify several potentials, denoted E_1 , E_2 , and E_3 , which are related to particular redox processes. We note that this is a stable CV in the sense that it does not change with further potential cycles.

In work [27], the potential E_1 was identified as formal potential of reaction (I) (see also [36]):



where Cit is the triply charged citrate anion. In a pH-neutral medium, this process can be written as:



We highlight that the formation of the indicated iron(III)–citrate complex occurred during preparation of the electrolyte to which an iron(II) salt was actually added (see Experimental). In our earlier work

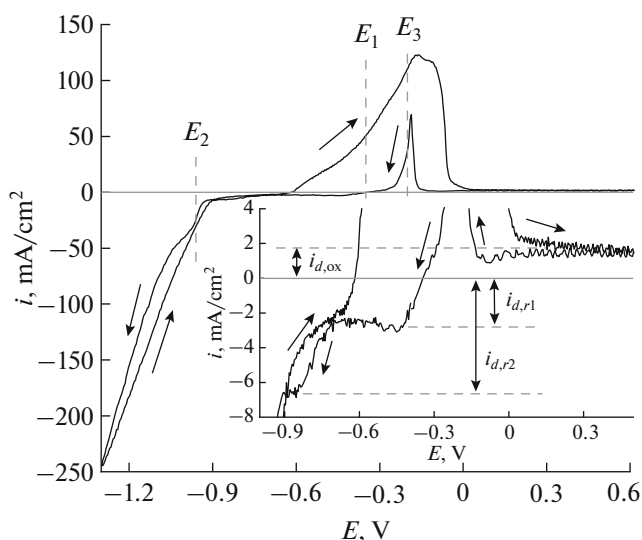


Fig. 1. CV characterizing electrodeposition of Fe–W alloys onto Pt electrode and their subsequent electroredissolution. Scan rate was 10 mV/s. Inset: magnified view of a part of CV.

[27], we showed that oxidation occurred even if the electrolyte solution was prepared in an inert gas atmosphere. Additionally, the ratio between iron–citrate complexes with different degrees of oxidation of the central ion(s) changed with time [26, 27]. We emphasize that the exact composition of these complexes and those indicated further in the text is not known. These could be polynuclear complexes, clusters, or more complex complexes [37–39]. The reactions indicated above and below in the text (Fig. 8) are rather schematic and reflect the nature and the direction of redox processes.

The rate of reduction of the citrate complex (current density $i_{d,r1}$, Fig. 1) is limited by mass transport [27], and, therefore, depends on the concentration of the Ox form and the electrode rotation rate. At applied current densities below $i_{d,r1}$, the entire charge passed through the electrode is spent on the reduction process (2), while the current efficiency of alloy electrodeposition is close to zero, which was confirmed experimentally (see below). As the potential is swept more cathodically, the citrate ion itself may undergo reduction, and the corresponding limiting current is $i_{d,r2}$ (Fig. 1 and see also Fig. 6a in work [27]). It is evident that the alloy electrodeposition (half-wave potential E_2 in Fig. 1) is complicated by reduction of oxidized forms such as the iron(III)–citrate complex and the citrate ion itself. If the current density due to reduction of the oxidized forms is denoted as i_{redox} , then the total current density i of the alloy deposition can be presented by the following formula:

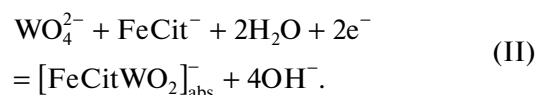
$$i = i_{redox} + i_{Fe} + i_W + i_H, \quad (1)$$

where i_{Fe} , i_W , and i_H are the partial current densities due to the formation of iron and tungsten, and the

evolution of hydrogen, respectively. The current density i_{redox} is dominant at low (total) current densities, with the consequence of the current efficiency of alloy electrodeposition falling to zero. At more negative potentials, i.e., beyond E_2 , the rate i_H of hydrogen evolution increases thus leading to a reduction in the current efficiency of alloy electrodeposition.

The current density i measured during potentiostatic electrodeposition (Fig. 2a) depended on the anode used. Transients shown in Fig. 2a correspond to a quite extended electrodeposition duration (2 h). It is clear that the current density starts growing after a certain amount of charge has passed, and, after a large amount of charge passed through the bath, then an actual increase in the current density depends on the chosen anode material, i.e., iron, graphite, or platinum.

The observed influence of the anode material can be rationalized by assuming that reduced forms present in the bath (e.g., iron–citrate complexes, possibly existing mixed iron–tungsten complexes, and the products of citrate ion reduction) undergo oxidation at different rates. This results in i_{redox} increasing, which, in turn, is anticipated to lead to lower current efficiencies of alloy electrodeposition in the galvanostatic mode. This conclusion is supported by current transients shown in Fig. 2b. The current density transients shown in this figure were recorded at a potential of -0.5 V that was applied before and after a 2-hour electrolysis using different anodes. We can see that i_{redox} went up by a factor of ~ 3 and ~ 2 in the cases of the platinum and graphite anodes, respectively, while for the soluble iron anode it rose by only ~ 15 – 20% . The data of Fig. 2 also indicate that the current efficiency of alloy electrodeposition varies with the deposition time and falls as the coating thickness increases in the case of insoluble anodes. Apart from reaction (Ia), however, other processes occur at $E > E_1$. After the electrode was poised at a potential of -0.5 V for 300 s and then reversed in the anodic direction, we registered a limiting current $i_{d,ox}$ (Fig. 1) associated with reaction (Ia), along with an anodic peak due to oxidation of the products deposited during the cathodic excursion of potential, the shape of this peak suggesting a process involving adsorbed species (Fig. 3). The amount of charge Q associated with this peak is 0.12 ± 0.03 C/cm². As was proposed in works [5, 6, 40] (see also [2]), it can be possible to describe the process of induced codeposition of Fe–W alloys by the reaction



Put differently, the iron(II) citrate (formed by reaction Ia) catalyzes reduction of tungsten species to give an intermediate that undergoes oxidation at a potential of -0.1 V. The amount of charge associated with oxidation of the formed surface layer is quite substantial. By our estimate, the layer thickness is ~ 30 nm.

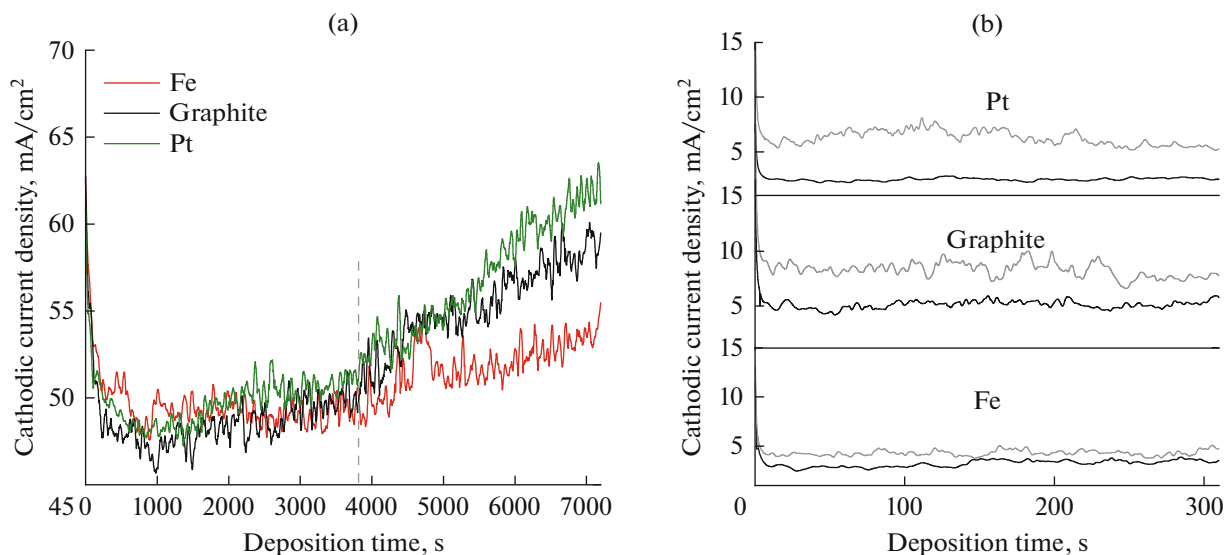


Fig. 2. Variations of cathodic current density with deposition time during potentiostatic depositions of Fe–W alloys on to Pt electrode using different anodes at different applied potentials: (a) -1.05 , and (b) -0.5 V. Electrodepositions were performed from a freshly prepared bath (black lines) or a bath previously used for plating at $E = -1.05$ V (b) for 2 h (gray lines).

The properties of this layer should become apparent in features of i_{redox} and, therefore, in different factors affecting the current density i of alloy electrodeposition. In particular, using electrochemical impedance spectroscopy for the ionic mass transfer in electrodeposition of Co–W alloy from a gluconate bath, it was shown that the current i depends, among other factors, on adsorption of intermediate species onto the electrode surface [41], and evidently this is the case here as well. The peak due to anodic oxidation of the reduction products formed during the cathodic process (Fig. 1) includes oxidation of products formed by both reactions (Ia) and (II) and anodic dissolution of the alloy deposited at the potential E_2 . The CV profile, on the backward scan, features a peak ($E_3 = -0.15$ V) corresponding to that process. The observation, that this peak disappears entirely after several subsequent anodic potential sweeps, assuming the starting potential was more positive than E_2 , supports the evidence that this is a peak due to anodic dissolution of the alloy.

Role of Anode Material in Electrodeposition of Fe–W Alloys: Investigating the Relationship between Current Efficiency and Cathodic Current Density

The dependences of current efficiency on the current density shown in Fig. 4 corroborate the conclusions reached earlier for Co–W coatings deposited from gluconate baths [8–11] and Fe–W coatings deposited from a citrate bath [33], namely, that the anode material has a considerable impact on the rate of cathodic electrodeposition of considered alloys. In contrast to our earlier works in which this conclusion was based on the results of relatively extended electro-

lysis (up to a few Ah/L), the results shown in Fig. 4 are for a bath age of less than 1 Ah/L. We see that the maximum current efficiency was reached using the iron anode. We note that the current efficiency data of Fig. 4 were calculated assuming that Fe was formed due to reduction of Fe(II) species (the alloy electrochemical equivalent was taken to be 1.09 g/Ah [27]). For comparison, a value obtained for the current efficiency for the case of the graphite anode is shown in Fig. 4 (dashed line); we note that this data are for a deposition in a cell with separated anode and cathode compartments. The current efficiency of Fe anodic disso-

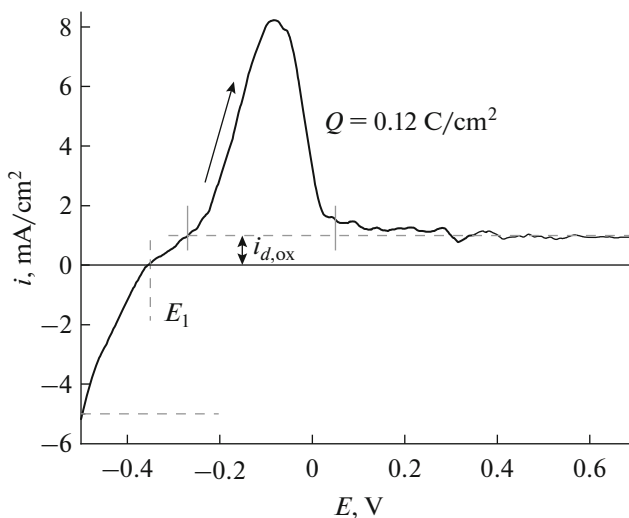


Fig. 3. Anodic polarization curve recorded on Pt electrode in considered bath. Prior to the potential sweep, the electrode was poised at a potential of -0.5 V for 300 s.

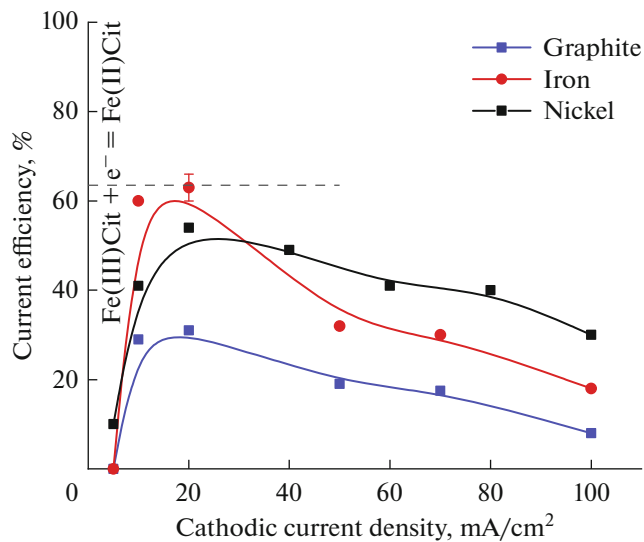


Fig. 4. Variations of cathodic current density with current efficiency for electrodeposition of Fe–W alloys using different anodes. Dashed line—current efficiency for Fe–W alloy electrodeposition in a cell with separate anode and cathode compartments, at applied current density of 20 mA/cm² using a graphite anode.

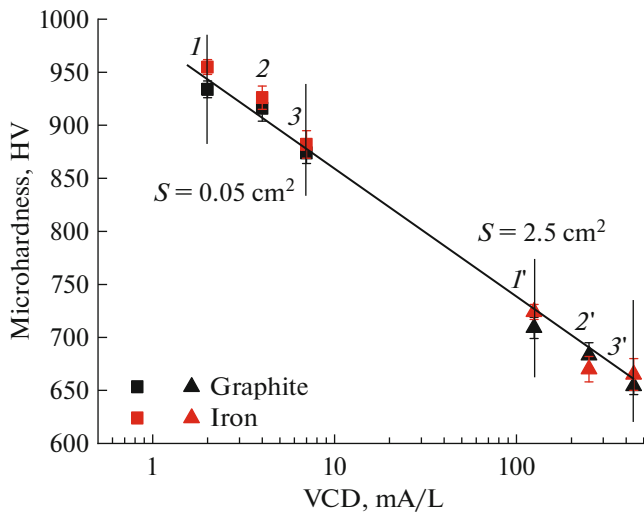


Fig. 5. Effect of VCD on microhardness of as-deposited Fe–W alloys. Coatings were electrodeposited at cathodic current densities of 20 (1, 1'), 40 (2, 2'), and 70 mA/cm² (3, 3') using different anodes and performing deposition on electrodes with different surface areas.

lution in this electrolyte was shown to be constant ($93 \pm 2\%$; assuming the formation of Fe(II) species) over a broad range of anodic current densities [27]. As for dissolution of a Ni anode in the same bath, specially designed experiments showed that the current efficiency was $\sim 90\%$ (assuming that the anode dissolves to give Ni(II) species). So, the maximum current efficiency was achieved when: (i) the iron anode

was used, and (ii) the anode and cathode compartments were separated.

Clearly, the observed behavior can be rationalized by assuming anodic oxidation of a metal complex directly involved in alloy deposition (an Fe(II)–citrate complex) and/or the ligand used (Fig. 2). With this process eliminated by using a cell with separate cathode and anode compartments or by replacing the oxidation process with anodic dissolution, the current efficiency reaches its maximum (Fig. 4). The current efficiency having maximum in a certain region of current densities is due to two factors: first, current densities below 10 mA/cm² at which the charge is mainly spent on reduction of an Fe(III)–citrate complex to a corresponding bivalent complex (Fe(II)–citrate) [27], which leads to the current efficiency falling to zero; and second, high current densities (> 40 mA/cm²) at which the charge is partly spent on the hydrogen evolution reaction and/or reduction of the organic species in the bath (e.g., the citrate ion).

Effect of Volume Current Density (VCD) on Microhardness of As-Deposited Fe–W Coatings

The use of soluble anodes, while having a considerable effect on the electrodeposition rate, has barely any impact on the microhardness of produced coatings (Fig. 5), which is mainly determined by the VCD, as was established in studies [7–12]. The composition of coatings does not depend on whether a soluble or an insoluble anode is used. For instance, an average tungsten content in the coatings deposited at a current density of 20 mA/cm² using a soluble iron anode was 29.5 ± 2.3 at %, while with a graphite anode it was 26.7 ± 1.7 at %. As a side note, the alloy composition was calculated from EDS data considering only its total metal content.

However, the data of Fig. 5 suggest that the microhardness of Fe–W coatings also depends on the VCD, regardless of the anode material. Those data are for coatings: (i) obtained at different electrodeposition current densities (20, 40, and 70 mA/cm²) and (ii) deposited onto substrates with different surface areas (0.05 and 2.5 cm²). Remarkably, they all fall on a single line showing the dependence of microhardness on the VCD (Figure 5). In particular, the size effect in microhardness is manifested as a dramatic change in the microhardness—from 950 to 725 HV—of coatings obtained at the same current density (20 mA/cm²) as the deposition surface area was enlarged from 0.05 to 2.5 cm² (Fig. 5).

The size effect in microhardness is related to the oxide content in the deposited coating, as was established for Co–W coatings deposited from a gluconate bath [12]. The oxides were found to accumulate only in surface layers of electroplated Co–W, Fe–W, and Ni–W alloys [42]. For Fe–W alloys electroplated from a glycolate–citrate bath, the incorporated oxygen was

found to be confined to only surface layers [43]. For a more detailed characterization of prepared Fe–W alloys electroplated from the citrate bath at a current density of 20 mA/cm² onto substrates with different surface areas (0.05 and 2.5 cm²), we carried out their XPS analysis.

The XPS depth profiles for the oxygen in prepared coatings are shown in Fig. 6, with the maximum depth being 200 nm and measurements made every ~7 nm. As can be seen, for the sample with a smaller deposition surface area (VCD = 2 mA/L), the incorporated oxygen is confined to a depth of ~30 nm, while for the sample obtained at a VCD of ~100 mA/L, the oxygen content is 2 at % or higher even at a depth of 200 nm below the sample surface. The data in Fig. 6 tell us that the oxygen-enriched layer is not uniform. Considering that such a layer can extend below the surface as deep as 1–1.5 μm [43] (in the cited work, coatings were deposited at a high VCD) and indents created at the surface as a result of microhardness measurements have similar depth, we can conclude that incorporation of oxygen leads to reduced microhardness. Moreover, if this layer with reduced microhardness is removed by mechanical polishing (Fig. 7), the VCD then has no effect on microhardness, i.e., after the oxide-rich layer is removed, the coating microhardness increases dramatically. Our data suggest that polishing of coatings deposited onto small-area substrates does not alter their microhardness (virtually independent of the applied current density of electrodeposition) since no oxygen was present in surface layers of such samples (Fig. 7).

Earlier studies related the effect of the VCD on the coating microhardness to the rate of variation of concentration of metal complexes directly involved in alloy deposition (here, it is an iron–citrate complex) [11, 12]:

$$v_i = \frac{\Delta c}{\tau} = \frac{c_i - c_x}{\tau} = \frac{\Delta m}{v\tau} = \frac{\varepsilon_i E_q I}{v}, \quad (2)$$

where $\Delta c = c_i - c_x$ is the variation of solution concentration of metal complexes involved in deposition, with c_i and c_x being the initial and current concentrations, respectively; τ is the time; ε_i is the current efficiency; E_q is the electrochemical equivalent; I is the current; and V is the electrolyte volume.

If we depart from the reaction scheme proposed in works [13–15] and another one in [5, 6, 40] and complement those with anodic processes described in [11, 12], then the overall reaction scheme can be given as that in Fig. 8.

In this diagram, illustrating the involved electrochemical processes, an Fe(II)–citrate complex is identified to play the key part in alloy deposition and is consumed in the following three reactions: reduction to metal iron (reaction (III)) via the formation of the intermediate Fe(OH)_{ads}, catalytic reduction to form metallic

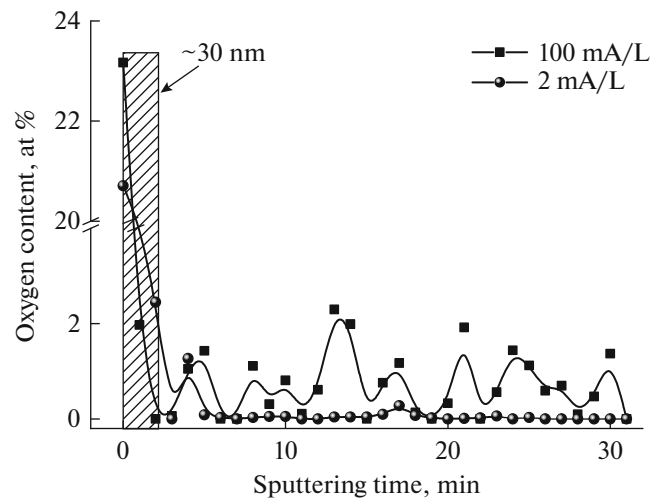


Fig. 6. XPS data showing the effect of VCD on the incorporation of oxygen in as-deposited Fe–W coatings: the oxygen depth profile for samples obtained at the indicated VCDs.

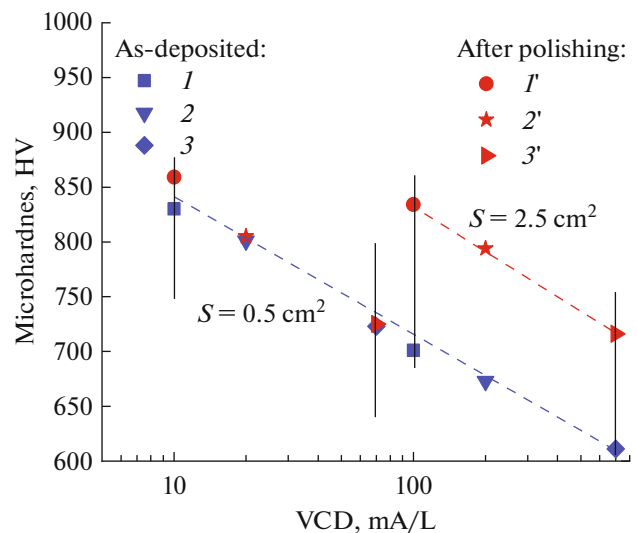


Fig. 7. Effect of VCD on microhardness of as-deposited Fe–W alloys. Coatings were obtained at cathodic current densities of –20 (I , I'), –40 (2 , $2'$), and –70 mA/cm² (3 , $3'$).

W (reactions (II) and (V) via the $[\text{FeCitWO}_2]_{\text{ads}}^-$ intermediate), and anodic oxidation at a Pt or graphite anodes (reaction (Ia)). If, however, the concentration of a metal complex involved in alloy deposition changes at a high rate (i.e., the VCD is high), the intermediate may undergo oxidation by water (reaction (VI)), thus favoring the formation of oxides and hydrogen absorption, which leads to a decrease in the coating microhardness. Both the iron anode dissolution (reaction (VII)) and the side reaction of hydrogen evolution

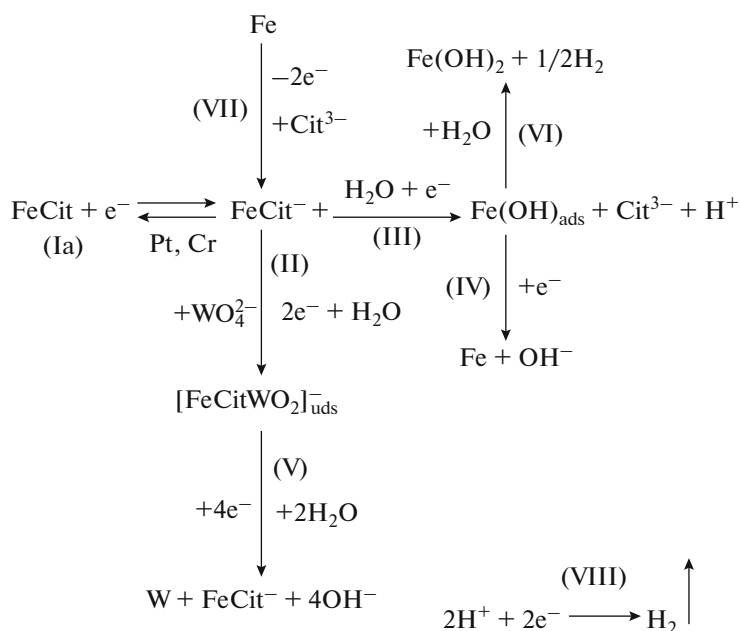


Fig. 8. Diagram of electrochemical processes involved in electrodeposition of Fe–W alloys from a citrate bath.

(reaction (VIII)) occur in parallel with these processes.

As the concentration of the metal complex involved in deposition (i.e., the concentration of an iron(II) complex) changes in a near-electrode layer increasingly faster, we anticipate the iron content in the coating to fall and, according to (1), the partial current i_{W} will increase at $i = \text{const}$. The carried out XPS analysis actually showed that at depths more than 30 μm the Fe content of coatings obtained at a high VCD was 68.7 ± 0.9 at %, while it was 73.4 ± 0.5 at % for coatings obtained at a low VCD.

A quantitative study of hydrogen absorption by the surface of Fe–W alloys deposited from citrate baths was conducted in [26]. The coatings obtained in that study were identified as Fe–W–H. The data on the hydrogen content in the coatings reported in [26] provide a qualitative support for the reaction diagram proposed herein and specifically for the effect of the VCD on coating microhardness. As the electrodeposition current density was raised from 10 to 50 mA/cm^2 , i.e., when the VCD grew by a factor of five while the electrodeposition area and the bath volume were constant, the hydrogen content in the coating increased from 0.4 to 12 cm^3/g [26].

Effects of Soluble Anode and Hydrodynamics on Deposition Rate and Composition of Fe–W Alloys

The variations of current efficiency with the current density recorded for different anodes (Fig. 4) suggest that, in the case of an average applied current density of 20 mA/cm^2 , the maximal deposition rate should

be at local current densities corresponding to x/h approximately in the range of 0.4–0.5 (see also Table 1). It is for these conditions that we observed the maximum deposition rate for a deposition onto an RCE in a Hull cell using a graphite anode (Fig. 9a). That being so, the deposition rate does not depend on the rotation rate at any current density. At low current densities, the observed dependence is due to the effects associated with i_{redox} (i.e., no alloy electrodeposition occurs at low current densities), while at high current densities this dependence is due to side reactions such as hydrogen evolution and reduction of organic components of the bath.

With the iron anode, the electrodeposition rate increases dramatically (Fig. 9b). For deposition in a quiescent bath, it reaches 33 $\mu\text{m}/\text{h}$, but it falls markedly as the rate of RCE rotation increases due to an increase in the diffusion-limited current associated with the reduction of the Fe(III)–citrate complex to the corresponding Fe(II)–citrate complex.

With the iron anode, the deposition rate can be substantially increased without any effect on the coating microhardness (Fig. 10). In addition, we can see that changes in the local current density do not affect HV values. The VCD has a decisive effect on the measured microhardness values. With the VCD increasing due to the average current density being raised from 20 to 40 mA/cm^2 (Fig. 10a, 10b), the coating microhardness falls from ~ 700 to ~ 600 kgf/mm^2 , albeit in both cases changes in the local current density had no effect on the measured HV values.

It is especially important to highlight that the local current density affects the distribution of tungsten in

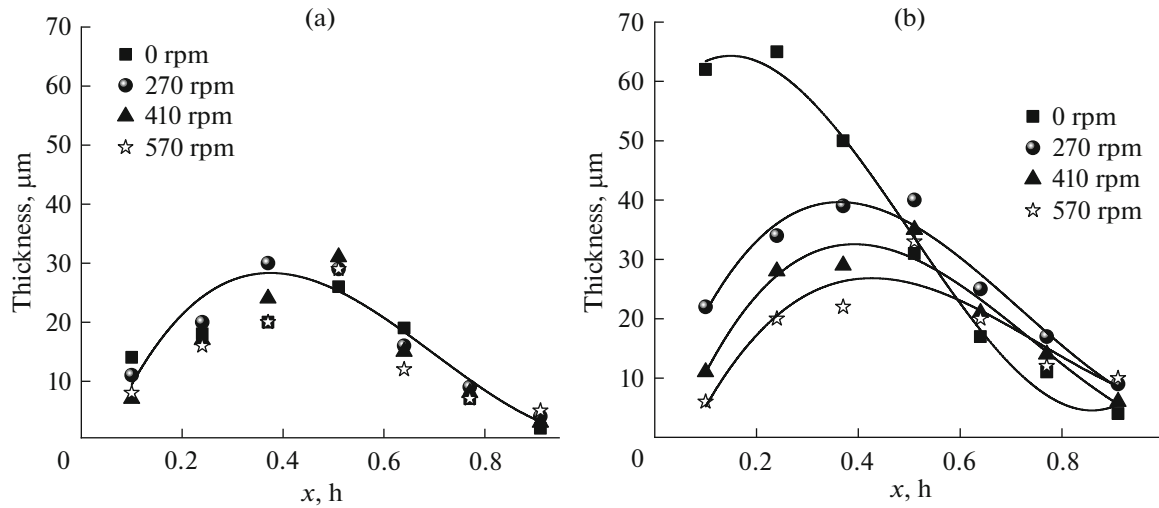


Fig. 9. Effect of local current density (RCH cell) and rotation speed on thickness of Fe–W coatings electrodeposited at current density of -20 mA/cm^2 for 2 h using different anodes: (a) graphite and (b) iron.

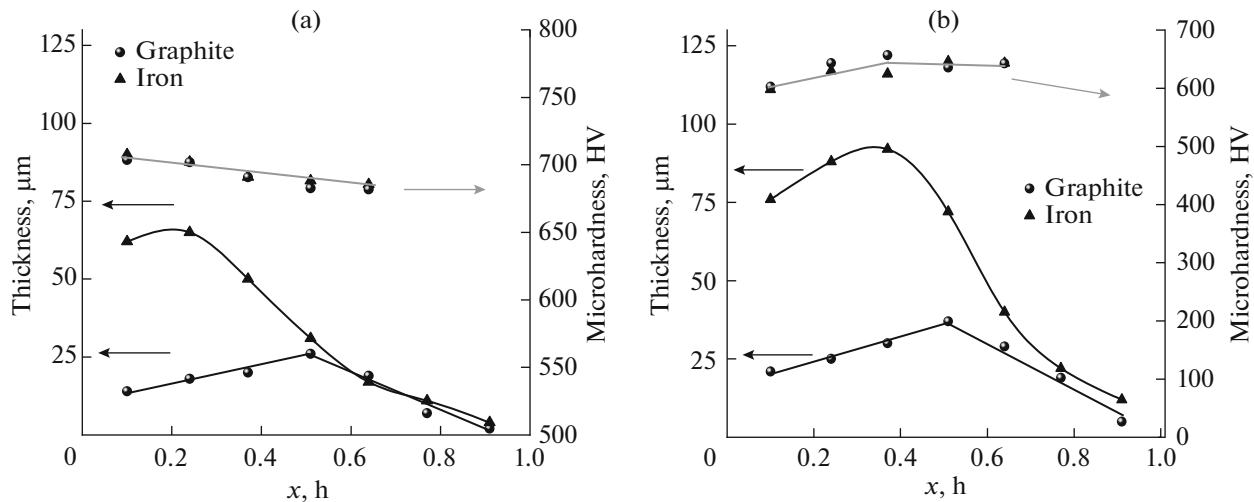


Fig. 10. Effect of local current density (RCH cell) on thickness and microhardness of Fe–W coatings electrodeposited at current density of: (a) -20 , and (b) -40 mA/cm^2 , for 2 h using different anodes.

the produced coatings (Fig. 11), which can vary broadly depending on the anode material and the local current density. According to (1), the partial current density for W electrodeposition can be expressed by the formula

$$i_W = i - i_{\text{redox}} - i_{\text{Fe}} - i_{\text{H}}. \quad (3)$$

That changes in the local current density have a considerable effect on the W content, while the microhardness remain unaffected, is a consequence of surface oxides being present in the coatings, which affects HV values measured experimentally. Their concentration, in turn, is a function of the rate of variation in the concentration of a metal complex involved in alloy deposition (Eq. (2)). It seems obvious that with the

surface oxide layer removed (as, for example, was done for some samples for which the data are shown in Fig. 7), the tungsten content in the coating must have a decisive impact on the coating microhardness.

Given the reaction diagram shown in Fig. 8, we can consider the partial current densities to be concurrent, since there is a competition between $(\text{FeOH})_{\text{ads}}$ and $[\text{FeCitWO}_2]_{\text{ads}}^-$ for surface sites (see also [40]). At the same time, the citrate complex FeCit^- directly involved in alloy deposition plays a double role: on the one hand, it catalyzes a reduction process leading to the formation of W, while on the other, it acts as precursor to the formation of Fe (and also oxides) in the alloy (Fig. 8). Reactions (II) and (IV) are not limited by its concentration, but the partial current of reduc-

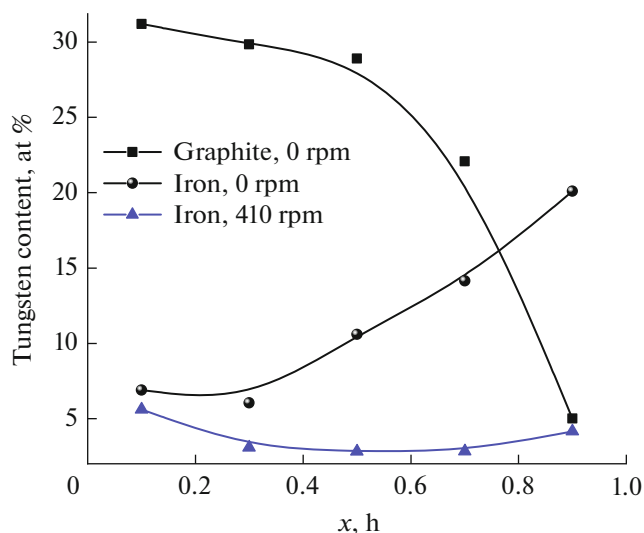


Fig. 11. Effect of local current density (expressed here as x/h ratio) and RCE rotation speed on W content in Fe–W coatings electrodeposited at current density of -20 mA/cm^2 for 2 h.

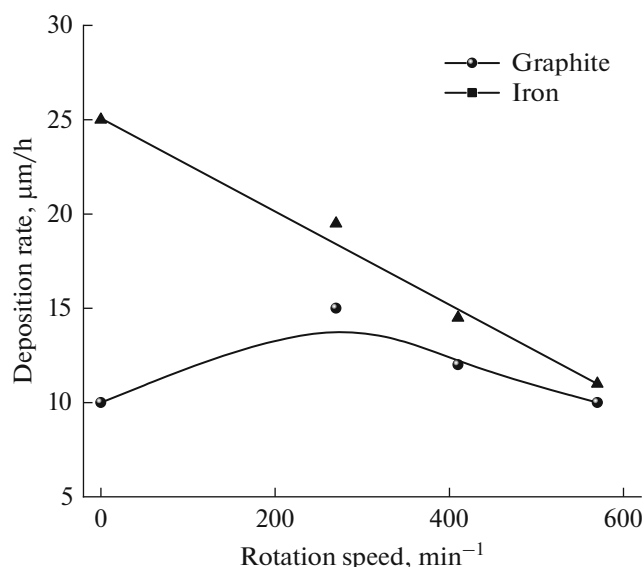


Fig. 12. Variations of Fe–W alloy deposition rate with rotation speed in RCH cell. Alloy deposition at cathodic current density of 20 mA/cm^2 using graphite or Fe anodes.

tion of iron species to elementary iron must grow with increasing this concentration, and the data of Fig. 11 support these conclusions. Equation (3) suggests that the alloy W content grows with increasing the electrodeposition current density and diminishes with increasing i_{redox} (i.e., with the rotation rate) and also i_{Fe} and i_{H} . All these trends were actually observed for depositions using the graphite anode (Fig. 11). The dependence of alloy W content on the local current density was markedly different in the case of the soluble iron anode because the concentration of the

Fe(II)–citrate complex grows especially if inter-electrode distances are small, as is the case for the Hull cell. With i_{Fe} increasing, the alloy W content falls accordingly, but it increases as the local current density of alloy deposition falls (Fig. 11). The trend for the alloy W content to fall as the rotation rate increases was particularly evident in experiments with the soluble (iron) anode since i_{redox} and i_{Fe} increased with the rotation rate ((3), Fig. 11). Nevertheless, the coating microhardness remained unaffected even if the alloy W content changed markedly (Fig. 10) since microhardness is determined by a layer of the surface oxide that results from chemical oxidation of the intermediate species $(\text{FeOH})_{\text{ads}}$ (Fig. 8).

The linear variation of the deposition rate for depositions at a current density of 20 mA/cm^2 is shown in Fig. 12. We note that those data were measured at $x/h = 0.37$, a point at which the local and average (applied) current densities coincide (see Table 1)), suggests that: (i) the observed deposition rate surpasses deposition rates reported elsewhere for Fe–W coatings [25] and (ii) that it drastically falls with increasing the rotation rate due to an increase in the diffusion-limited current of the side reaction of Fe(III)–citrate complex reduction. However, reaction (1a) should not be considered to be a side reaction, because it gives rise to a catalyst for reduction of tungsten species and to a precursor to the formation of iron in the coating (Fig. 8). Considering the specific features of the electrochemical system under study when using a soluble Fe anode, i.e., an increase in the deposition rate with the applied current density, it is promising for local, mask-free electrodeposition [44].

CONCLUSIONS

(1) We showed that a citrate bath for plating Fe–W alloys contains different citrate complexes of bi- and trivalent iron, along with its main components, i.e., an Fe(II) salt and sodium tungstate.

(2) For this bath, the current efficiency of alloy electrodeposition was found to depend on the anode material. It reaches a maximum of $\sim 63\%$ (assuming deposition from Fe (II) and W(VI) species) if the cathode and anode compartments are separated or a soluble iron anode is used.

(3) Reduction of the Fe(III) complex to its Fe(II) counterpart is the dominant electrode process at low current densities ($< 10 \text{ mA/cm}^2$), which leads to the current efficiency of alloy deposition dwindling to zero. The reduction process is under mixed kinetic control, i.e., diffusion complicated by adsorption of an intermediate species (a layer of $\sim 30 \text{ nm}$ containing Fe and W). This layer is formed due to a catalytic reduction of a tungsten complex mediated by an Fe(II)–citrate complex, a catalyst, resulting from reduction of an Fe(III)–citrate complex at the electrode surface.

(4) The metal complex directly involved in alloy deposition (a citrate–Fe(II) complex) undergoes oxidation at the anode. The rate of this process depends on the anode material, which leads to: (i) an increase in the limiting current density of reduction of oxidation products, and (ii) the anode material affecting the current efficiency and the rate of alloy electrodeposition.

(5) This complex, apart from undergoing oxidation at the anode and acting as catalyst in the reduction of tungsten species, is reduced to metallic iron via the formation of the $\text{Fe}(\text{OH})_{\text{ads}}$ intermediate. The process can unfold along two different paths, depending on the rate the concentration of the complex under discussion changes with: it is either formation of metallic iron or oxidation of the intermediate by water to yield oxy-hydroxides, with the alloy absorbing the formed hydrogen. For cases of high rates of variation in the concentration of this complex (i.e., at high VCDs), the XPS analysis showed an elevated oxygen content in the alloys, while at low VCDs, oxygen was confined to a surface layer ~ 30 nm thin. At high VCDs, the oxygen-containing layer extends 1–1.5 μm deep, a range of depths comparable to that of indents made during microhardness measurements. With this layer removed, the VCD had no effect on the coating microhardness.

(6) The partial currents associated with the formation of tungsten (i_{W}) and iron (i_{Fe}) and hydrogen evolution (i_{H}) and the total current due to reduction of oxidized species (i_{redox}) depend on the surface coverage with the corresponding intermediates. With a soluble iron anode, the total current drastically increases due to an increase in i_{Fe} , which, in turn, leads to a lower tungsten content in the deposited alloy. This, however, does not affect the alloy microhardness because it is determined by VCD, i.e., the concentration of oxides in the surface layer.

(7) By using a soluble iron anode, it was possible to achieve a maximum deposition rate in a quiescent bath: 25 $\mu\text{m}/\text{h}$ at an applied current density of 20 mA/cm^2 . With forced convection, the deposition rate fell due to an increase in the limiting current i_{redox} associated with reduction of oxidized species.

(8) Because the alloy deposition rate increases markedly with the current density (within a certain range of current densities), the considered system is promising for use in mask-free, local electro-deposition.

FUNDING

This work was supported by the budget of the institutional project of the Institute of Applied Physics “Physico-chemical Methods for Obtaining New Materials and Surfaces for Multiscale Technologies” (no. 15.817.02.05A), the H2020 project “Smartelectrodes” (no. 778357), and by Shevchenko Pridnestrovie State University.

REFERENCES

1. Eliaz, N. and Gileadi, N., *Mod. Aspects Electrochem.*, 2008, vol. 42, pp. 191–301.
https://doi.org/10.1007/978-0-387-49489-0_4
2. Tsyntaru, N., Cesiulis, H., Donten, M., Sort, J., et al., *Surf. Eng. Appl. Electrochem.*, 2012, vol. 48, no. 6, pp. 491–520.
<https://doi.org/10.3103/s1068375512060038>
3. Cesiulis, H., Tsyntaru, N., Podlaha, E., Li D., et al., *Curr. Nanosci.*, 2018, vol. 14, pp. 1–16.
<https://doi.org/10.2174/1573413714666180410154104>
4. Brenner, A., *Electrodeposition of Alloys: Principle and Practice*, New York: Academic, 1963.
<https://doi.org/10.1016/b978-1-4831-9807-1.50032-5>
5. Podlaha, E.J. and Landolt, D., *J. Electrochem. Soc.*, 1996, vol. 143, pp. 884–893.
<https://doi.org/10.1149/1.1836554>
6. Podlaha, E.J. and Landolt, D., *J. Electrochem. Soc.*, 1996, vol. 143, pp. 893–896.
<https://doi.org/10.1149/1.1836554>
7. Silkin, S.A., Gotelyak, A.V., Tsyntaru, N.I., and Dikumar, A.I., *Surf. Eng. Appl. Electrochem.*, 2015, vol. 51, no. 3, pp. 228–234.
<https://doi.org/10.3103/s106837551503014x>
8. Belevskii, S.S., Bobanova, Zh.I., Buravets, V.A., Gotelyak, A.V., et al., *Russ. J. Appl. Chem.*, 2016, vol. 89, no. 9, pp. 1427–1433.
<https://doi.org/10.1134/s107042721609007x>
9. Gotelyak, A.V., Silkin, S.A., Yahova E.A., and Dikumar, A.I., *Russ. J. Appl. Chem.*, 2017, vol. 90, no. 4, pp. 541–546.
<https://doi.org/10.1134/s1070427217040085>
10. Silkin, S.A., Gotelyak, A.V., Tsyntaru, N.I., and Dikumar, A.I., *Surf. Eng. Appl. Electrochem.*, 2017, vol. 53, no. 1, pp. 6–13.
<https://doi.org/10.3103/s1068375517010136>
11. Danil'chuk, V.V., Silkin, S.A., Gotelyak, A.V., Buravets, V.A., et al., *Russ. J. Electrochem.*, 2018, vol. 54, no. 11, pp. 930–936.
<https://doi.org/10.1134/s1023193518130116>
12. Belevskii, S.S., Gotelyak, A.V., Silkin, S.A., and Dikumar, A.I., *Surf. Eng. Appl. Electrochem.*, 2019, vol. 55, no. 1, pp. 46–52.
<https://doi.org/10.3103/s1068375519010058>
13. Krasikov, V.L., *Byull. S-Peterb. Gos. Tekh. Univ.*, 2015, no. 31, pp. 40–43.
<https://doi.org/10.15217/issn1998984-9.2015.31.40>
14. Krasikov, V.L. and Krasikov, A.V., *Byull. S-Peterb. Gos. Tekh. Univ.*, 2016, no. 36, pp. 12–23.
<https://doi.org/10.15217/issn1998984-9.2016.36.12>
15. Krasikov, A.V. and Krasikov, V.L., *Byull. S-Peterb. Gos. Tekh. Univ.*, 2016, no. 37, pp. 8–14.
<https://doi.org/10.15217/issn1998984-9.2016.37.8>
16. Holt, L. and Black, R., *J. Electrochem. Soc.*, 1942, vol. 82, no. 1, p. 205.
<https://doi.org/10.1149/1.3071408>
17. Brenner, A., Burkhead, P.S., and Seegmiller, E., *J. Res. Bur. Stand.*, 1947, vol. 39, pp. 351–383.
<https://doi.org/10.6028/jres.039.023>

18. Donten, M., Cesiulis, H., and Stojek, Z., *Electrochim. Acta*, 2000, vol. 45, pp. 3389–3396. doi 00437-0
[https://doi.org/10.1016/s0013-4686\(00\)00437-0](https://doi.org/10.1016/s0013-4686(00)00437-0)
19. Gamburg, Yu., Zahkarov, E., and Gorynov, G., *Russ. J. Electrochem.*, 2001, vol. 37, pp. 670–673.
<https://doi.org/10.1023/a:1016752231015>
20. Tsyntsaru, N., Bobanova, J., Ye, X., Cesiulis, H., et al., *Surf. Coat. Technol.*, 2009, vol. 203, pp. 3136–3141.
<https://doi.org/10.1016/j.surfcoat.2009.03.041>
21. Bobanova, Zh.I., Dikusar, A.I., Cesiulis, H., Celis, J.-P., et al., *Russ. J. Electrochem.*, 2009, vol. 45, pp. 895–901.
<https://doi.org/10.1134/s1023193509080096>
22. He, F., Yang, J., Lei, T., and Gu, C., *Appl. Surf. Sci.*, 2007, vol. 253, pp. 7591–7598.
<https://doi.org/10.1134/s1023193509080096>
23. Yermolenko, I.Y., Ved, M.V., Sakhnenko, N.D., and Sachanova, Y.I., *Nanoscale Res. Lett.*, 2017, vol. 12, no. 1, p. 352.
<https://doi.org/10.1186/s11671-017-2128-3>
24. Yar-Mukhaamedova, G., Ved, M., Sakhnenko, N., Karakurkchi, A., et al., *Appl. Surf. Sci.*, 2016, vol. 383, pp. 346–352.
<https://doi.org/10.1016/j.apsusc.2016.04.046>
25. Nicolenco, A., Tsyntsaru, N., and Cesiulis, H., *J. Electrochem. Soc.*, 2017, vol. 164, no. 9, pp. D590–D596.
<https://doi.org/10.1149/2.1001709jes>
26. Gamburg, Yu.D. and Zaharov, E.N., *Surf. Eng. Appl. Electrochem.*, 2019, vol. 55, no. 4, pp. 402–409.
<https://doi.org/10.3103/s1068p75519040033>
27. Belevskii, S.S., Gotelyak, A.V., Yuschenko, S.P., and Dikusar, A.I., *Surf. Eng. Appl. Electrochem.*, 2019, vol. 55, no. 2, pp. 119–129.
<https://doi.org/10.3103/s1068375519020054>
28. Thangaraj, N., Tamilarasn, K., and Sasikumar, D., *Indian J. Pure Appl. Phys.*, 2014, vol. 52, pp. 395–398.
29. Kuznetsov, V., Golyanin, K., and Pshenichkina, T., *Russ. J. Electrochem.*, 2012, vol. 52, pp. 1107–1112.
<https://doi.org/10.1134/s1023193512110109>
30. Wang S., Zeng C., Ling Y., Wang J., et al., *Surf. Coat. Technol.*, 2016, vol. 286, pp. 36–41.
<https://doi.org/10.1016/j.surfcoat.2015.12.011>
31. Tsyntsaru, N., Bobanova, Zh.I., Kroitoru, D., Cheban, V.F., et al., *Surf. Eng. Appl. Electrochem.*, 2010, vol. 46, pp. 346–352.
<https://doi.org/10.3103/s1068375510060025>
32. Nicolenco, A., Tsyntsaru, N., Fornell, J., Pellicer, E., et al., *Mater. Des.*, 2018, vol. 139, pp. 429–438.
<https://doi.org/10.1016/j.matdes.2018.07.038>
33. Ishida, K., Morikawa, T., Miyake, M., and Hirato, T., *J. Surf. Finish Soc. Jpn.*, 2016, vol. 67, no. 9, pp. 489–493. doi 104139/stj.67.489
34. Madore, C., West, A.C., Matlosh, H., and Landolt, D., *Electrochim. Acta*, 1992, vol. 37, no. 1, p. 69.
[https://doi.org/10.1016/0013-4686\(92\)80013-c](https://doi.org/10.1016/0013-4686(92)80013-c)
35. Silkin, S.A., Belevskii, S.S., Gradinar, A., et al., *Surf. Eng. Appl. Electrochem.*, 2010, vol. 46, no. 3, pp. 206–214.
<https://doi.org/10.3103/s1068375510030026>
36. Cox, J. and Cummings, E.A., *J. Electroanal. Chem.*, 1973, vol. 42, pp. 153–157.
[https://doi.org/10.1016/s0022-0728\(73\)80087-7](https://doi.org/10.1016/s0022-0728(73)80087-7)
37. Belevskii, S.S., Yushchenko, S.P., and Dikusar, A.I., *Surf. Eng. Appl. Electrochem.*, 2012, vol. 48, no. 1, pp. 97–98.
<https://doi.org/10.3103/s1068375512010036>
38. Belevskii, S.S., Buravets, V.A., Yushchenko, S.P., Zgardan, I.M., et al., *Surf. Eng. Appl. Electrochem.*, 2016, vol. 52, no. 4, pp. 350–355.
<https://doi.org/10.3103/s1068375516040049>
39. Belevskii, S.S., Buravets, V.A., Yushchenko, S.P., and Dikusar, A.I., *Surf. Eng. Appl. Electrochem.*, 2016, vol. 52, no. 5, pp. 420–426.
<https://doi.org/10.3103/s1068375516050057>
40. Sun, S., Bairachna, T., and Podlaha, E.J., *J. Electrochem. Soc.*, 2013, vol. 160, no. 10, pp. D434–D440.
<https://doi.org/10.1149/2.014310jes>
41. Belevskii, S.S., Cesiulis, H., Tsyntsaru, N., and Dikusar, A.I., *Surf. Eng. Appl. Electrochem.*, 2010, vol. 46, no. 6, pp. 570–578.
<https://doi.org/10.3103/s1068375510060050>
42. Donten, M., *J. Solid State Electrochem.*, 1999, vol. 3, pp. 87–96.
<https://doi.org/10.1007/s100080050133>
43. Mulone, A., Nicolenco, A., Hoffmann, V., Klement, U., Tsyntsaru, N., et al., *Electrochim. Acta*, 2018, vol. 261, pp. 167–177.
<https://doi.org/10.1016/j.electacta.2017.12.051>
44. Volgin, V.M., Kabanova, T.B., and Davydov, A.D., *Chem. Eng. Sci.*, 2018, vol. 183, pp. 123–135.
<https://doi.org/10.1016/j.ces.2018.03.019>